Effect of solid rubber fenders on the structural damage due to collisions between a ship-shaped offshore installation and an offshore supply vessel

Hye Rim Cho[a], Hyeong Jin Kim[b], Sang Min Park [a], Dae Kyeom Park [c], Soon Hwan Yun[d], Jeom Kee Paik[b,c,e*]

[a]Department of Naval Architecture and Ocean Engineering, Pusan National University, Busan, Republic of Korea

[b]Department of Mechanical Engineering, University College London, London, UK

[c]The Korea Ship and Offshore Research Institute (Lloyd's Foundation Research Centre of Excellence), Pusan National University, Busan, Republic of Korea

[d]Fender Engineering Team, Hwaseung Corporation, Busan, Republic of Korea

[e]School of Maritime and Transportation, Ningbo University, Ningbo, People's Republic of China

* Corresponding author: Jeom Kee Paik. Email: j.paik@ucl.ac.uk

Abstract

The effect of solid rubber fenders on the structural damage due to collisions between a ship-shaped offshore installation and an offshore supply vessel was investigated. An LS-DYNA computational modelling technique was developed to simulate the kinetic energy absorption behaviour of solid rubber fenders. Physical crushing testing was performed on rubber fender models to validate the computational model under different collision speeds. Traditional LS-DYNA computational models to simulate the structural crashworthiness of ship-shaped offshore hull structures colliding with an offshore supply vessel were combined with the developed rubber fender model. The computational models were applied to a hypothetical very-large-crude-carrier (VLCC) class floating production storage and offloading (FPSO) unit hull that collides with an offshore supply vessel equipped with rubber fenders in the forecastle deck area, and the effects of rubber fenders on the collision energy absorption characteristics were examined in association with the structural damage of both striking OSV and struck FPSO hull structures. The findings and insights derived from the study were summarised.

Keywords: structural crashworthiness, ship-shaped offshore installations, offshore supply vessels (OSV), solid rubber fender, collision damage

1. Introduction

Despite various efforts to prevent the structural damage caused by collisions between ships or between offshore installations and supply vessels, collisions may still occur owing to harsh environmental conditions, operational error, human error, and equipment failure. Consequently, safety studies must be performed when designing ships and offshore installations, and effective methods to protect the hull of ships from accidents must be developed as accidents may lead to significant damage such as human casualties, financial loss, and environmental pollution (Paik 2020, 2022). Notably, the mechanisms of structural responses in accidents are highly nonlinear and non-Gaussian and involve multiple physical processes, scales, and criteria, owing to which the resolution and evaluation of the associated issues are complex. In addition, a highly accurate model is required to quantitatively compute the load effects for a collision scenario because the structural responses in such events may be volatile, uncertain, complex, and ambiguous.

In this context, several researchers have attempted to evaluate the load effect in collision accidents. Pedersen and Zhang (1998) suggested a probabilistic calculation model for the collision-induced damage of ship structures. Ozguc (2020a, 2020b) proposed an approach to assess the hull strength in collision situations and the amount of damage to offshore installations equipped with crash protection devices on the FPSO hull. Fan et al. (2020) developed a simplified analytical method to efficiently predict the protective performance of steel fenders in ship-to-ship collision scenarios. Fernandez et al. (2021) evaluated the collision between an offshore supply vessel (OSV) and floating production storage and offloading (FPSO) platform. Park et al. (2022) investigated the effects of pneumatic rubber fenders on the prevention of structural damage from collisions between a ship-shaped offshore installation and a shuttle tanker during side-by-side offloading operations. Notably, unlike for steel materials, no technique to model the dynamic properties of rubber materials has been established. Moreover, the structural crashworthiness analysis considering the properties of rubber fenders is limited.

Considering these aspects, this study quantitatively evaluated the structural crashworthiness in ship-to-ship collision events with rubber fenders installed on the colliding entities. Before the ship-to-ship collision analysis, physical model testing was performed to investigate the

kinetic energy absorption performance of the rubber fenders, and computational model techniques using the LS-DYNA nonlinear finite element analysis program were developed to perform numerical analyses. The results of the physical crushing testing and simulation of the rubber fender were compared to validate the computation modelling.

The developed computational models were applied to the analysis of structural crashworthiness in collision events between a VLCC class FPSO hull (struck body) and an OSV (striking body) using the LS-DYNA code. Table 1 presents the principal dimensions of the striking and struck bodies. The finite element method (FEM) analysis for the structural crashworthiness was conducted by applying various collision speed conditions in situations in which the bow of an OSV collides with the side of an FPSO unit. In addition, the structural crashworthiness was compared from various perspectives via simulations of ship-to-ship collisions, with the colliding entities equipped or not equipped with rubber fenders. Table 2 summarises a total of eight collision conditions considered in the present study.

Table 1. Principal dimensions of OSV and FPSO.

Particulars	FPSO	OSV
Length of all (m)	305.0	99.7
Breadth (m)	60.0	23.3
Draught (m)	23.3	7.1
Displacement (ton)	VLCC	8,546
Load condition	Full	Full

Table 2. Study cases with different collision conditions between a striking 8,546-ton OSV and a struck VLCC class FPSO.

Case no.	Collision speed (m/s)	Rubber fender
1	1.03 (2 kt)	Not equipped
2		Equipped
3	2.06 (4 kt)	Not equipped
4		Equipped
5	3.09 (6 kt)	Not equipped
6		Equipped
7	4.12 (8 kt)	Not equipped
8		Equipped

2. Crashworthiness of a solid rubber fender

2.1 Properties of rubber material

Table 3 shows the properties of solid rubber material considered in the present study. The tensile test was conducted to determine the mechanical properties of rubber material used for the present experiment of solid rubber fenders. Figure 1 shows the shape and dimensions of a rubber specimen that meets the ASTM D 412 standard where the gauge length is 20 mm. Figure 2 shows the test set-up of universal testing machine (Instron 5565) in which the maximum loading capacity is 1 kN and the maximum loading speed is 500 mm/min. In the test, loading speed was varied at 3, 60, and 500 mm/min. Figure 3 shows the test results on the relationship between engineering stress versus engineering strain. Table 4 summarises the test results in terms of mechanical properties of rubber material. As rubber does not have a distinct (critical) stress (e.g., yield stress), a reference stress was measured at a strain of 1 mm/mm as indicated in Table 4.

Because of the limitation of the test machine in capacity, the loading speed was applied up to 500 mm/min, which is equivalent to a strain rate of 0.417/s. It is expected that the strain rates in real collisions can be much larger. In this regard, an extrapolation of the present test data was undertaken to predict the region of larger strain rates up to a strain rate of 100/s, as shown in Figure 4, where an obvious trend of straight line is observed between stress versus logarithmic strain rate. Figure 5 shows the relationship between engineering stress versus engineering strain with varying strain rates where both the test data in small strain rate region and the data so predicted in large strain rate region are plotted altogether.

Table 3. Material properties of solid rubber material.

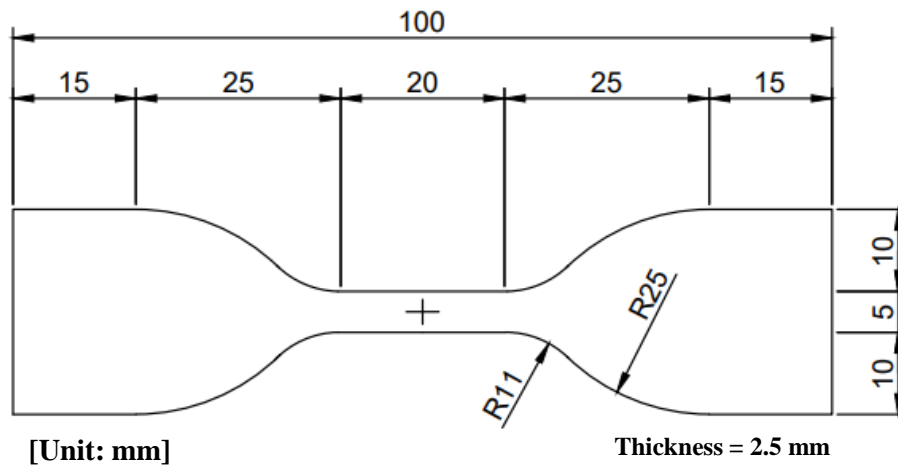| Feature	Value
Material type	Vulcanised rubber
Density (kg/m^3)	1.18
Poisson's ratio	0.49
Bulk modulus (MPa)	1,250

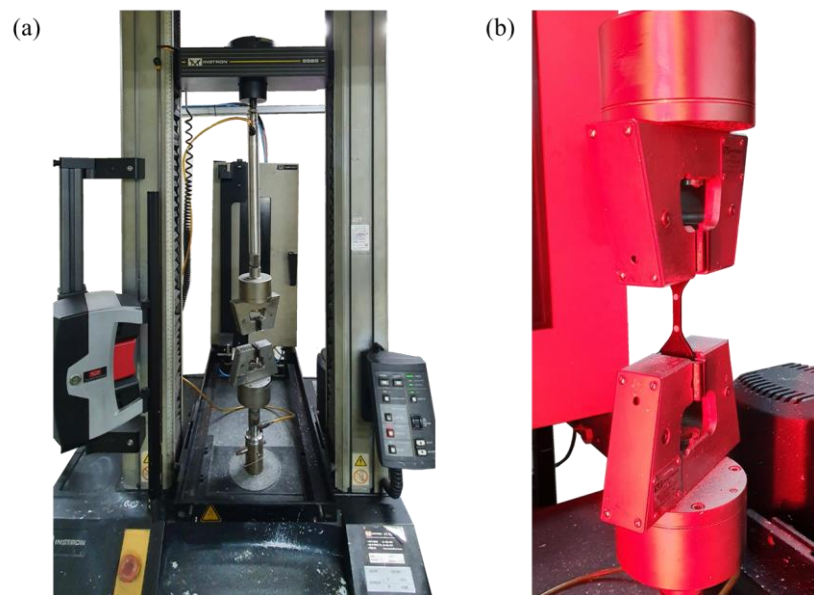Figure 1. Tensile coupon test specimen of rubber material per ASTM D 412 standard.

Figure 2. Instron 5565 universal test machine for tensile coupon testing with varying loading speed: (a) Test set-up, (b) Test specimen installation.
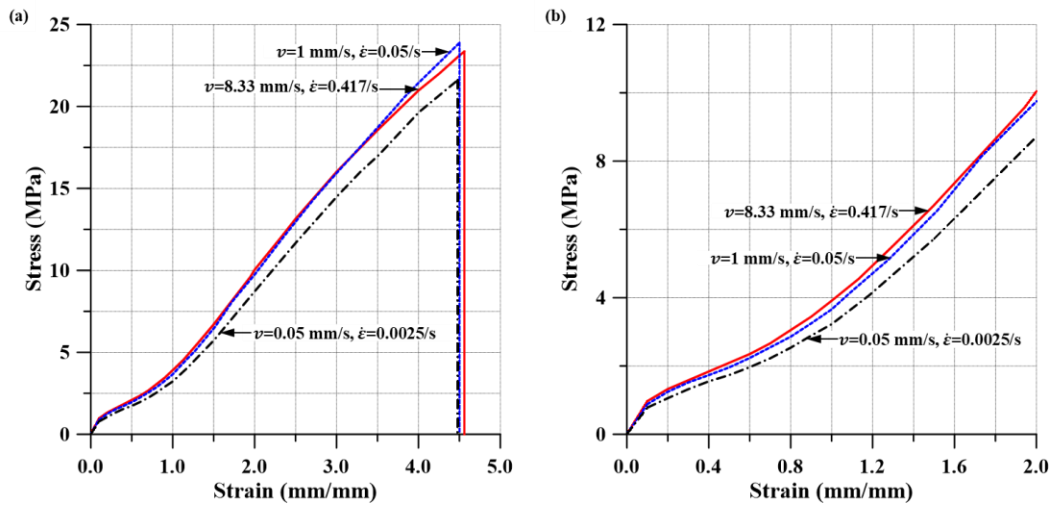
Figure 3. Results of tensile coupon test: (a) Entire behaviour until rupture, (b) Enlarged behaviour up to a strain of 200 % (v = loading speed, $\dot{\varepsilon}$ = strain rate).

Table 4. Mechanical properties of rubber material.

Loading speed (mm/min)	Strain rate (1/s)	Fracture strain	Average of fracture strain	Reference stress (MPa) at strain of 1mm/mm	Elastic modulus (MPa)
3	0.0025	4.48		3.22	7.76
60	0.05	4.50	4.51	3.66	-
500	0.417	4.56		3.91	-
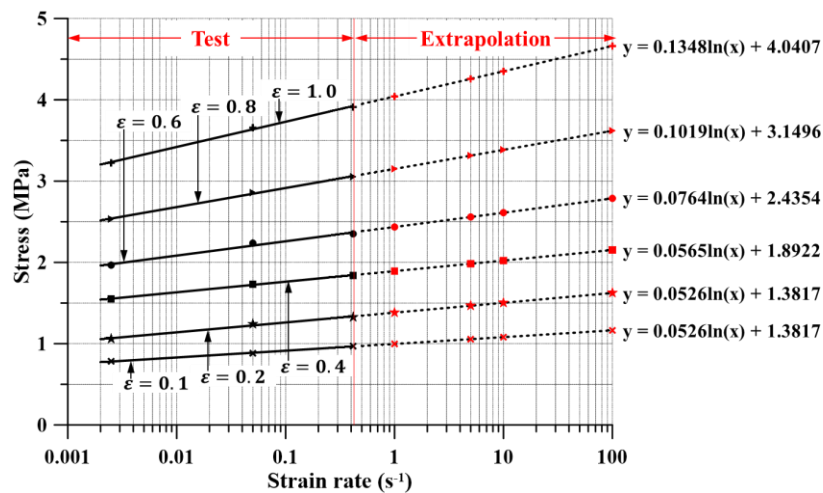
Figure 4. An extrapolation of the test data to predict the region of larger strain rates (ε = engineering strain).
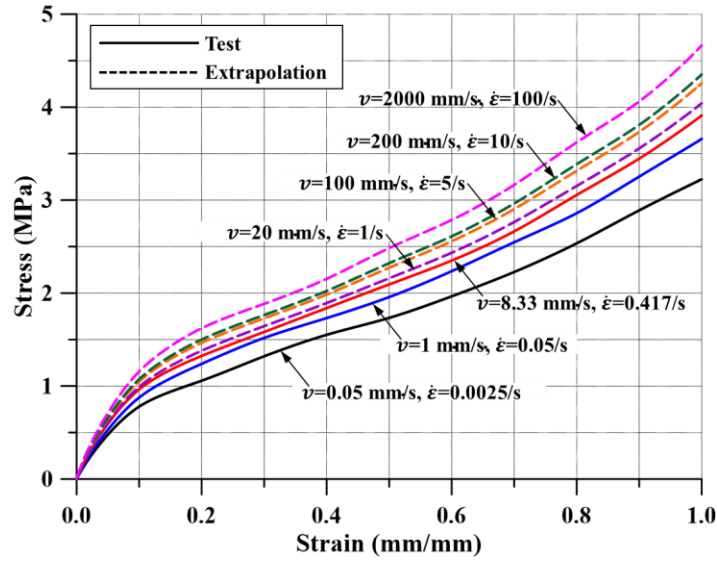
Figure 5. Relation between engineering stress and engineering strain with varying strain rates (v = loading speed, $\dot{\varepsilon}$ = strain rate).

2.2 Crushing test on a solid rubber fender

Crushing testing was conducted on a cylindrical solid rubber fender to characterise the crashworthiness in impact loading. Figure 6 and Table 5 present the shape and dimensions of the tested rubber fender, produced by Hwaseung Corporation in South Korea. Dimensions were measured at four points of circumference and their average was considered in the computational simulations.
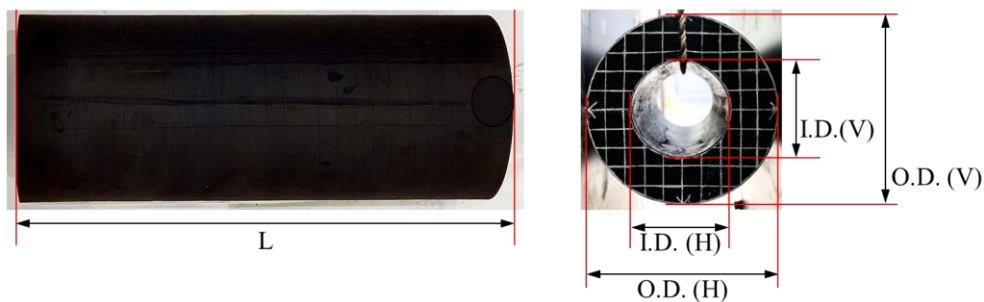
Figure 6. Shape of the tested rubber fender, produced by Hwaseung Corporation.

Table 5. Dimensions of the tested rubber fender (the indicated diameter is the average of both end dimensions).

Measurement	Length (L) (mm)	Vertical diameter (mm)		Horizontal diameter (mm)	
		Outside (O.D. (V))	Inner (I.D. (V))	Outside (O.D. (H))	Inner (I.D. (H))
1	1,000	398.5	196.7	404.6	206.7
2		401.1	200.8	400.3	202.0
3		401.1	201.4	400.3	202.7
4		398.7	199.8	404.0	205.5
Average	1,000	399.9	199.7	402.3	204.2

As shown in Figure 7, the testing was performed under compressive loading in the horizontal direction of a cylindrical fender, where the loading speed was varied to investigate the dynamic behaviour of the rubber fender. Figures 8 shows the test set-up using the dynamic test loading actuator at the ICASS/KOSORI in Hadong, South Korea, see Chapter 18 of Paik (2020). Figure 9 schematically illustrates the equipment designed to conduct the test and application of the load in the axial direction of the hydraulic actuator. The hydraulic actuator was fixed to the reaction force wall. Wheels installed under the compression plate were used to fix the actuator alignment and minimize unnecessary friction. The load speed and displacement were controlled through a personal computer connected to a hydraulic actuator. The applied load history was output through the load cell of the actuator.

The conditions in four different cases are summarised in Table 6, where the load speed was kept constant up to a maximum penetration of 200 mm. The same fender was used for different testing at different loading speeds because of the cost issue. As testing was performed on only one specimen, however, a rest period of at least 20 min was maintained between tests to ensure specimen recovery. It is known that the stiffness of rubber products subjected to cyclic loading decreases due to the so-called Mullins effect (Mullins 1969) or softening effect, but a total of five-cycle crushing tests do not affect the responses significantly at small deformations, as shown in Figure 10, where the loading speed was 200 mm/s. However, further study is recommended to investigate the softening effect of rubber material due to more repeated loading cycle causing large deformations.

The test results at different loading speeds are presented in section 2.4 where the computed results are compared with test data.
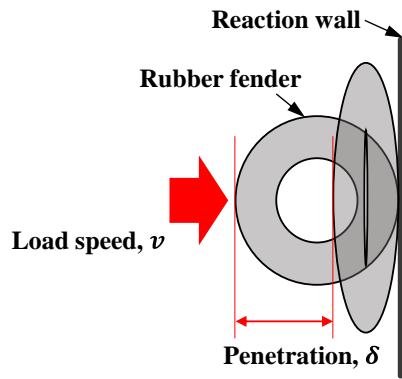
Figure 7. Schematic of loading and penetration in the horizontal direction of a cylindrical solid rubber fender applied in the test.
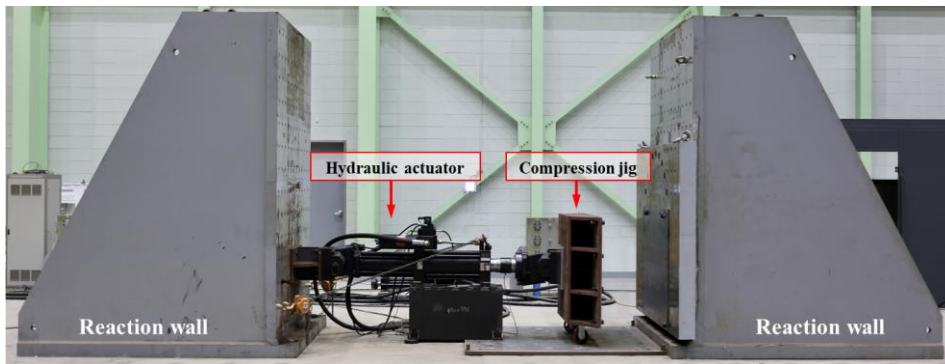

Figure 8. Crushing test set-up at the test site of the ICASS/KOSORI in Hadong, South Korea.
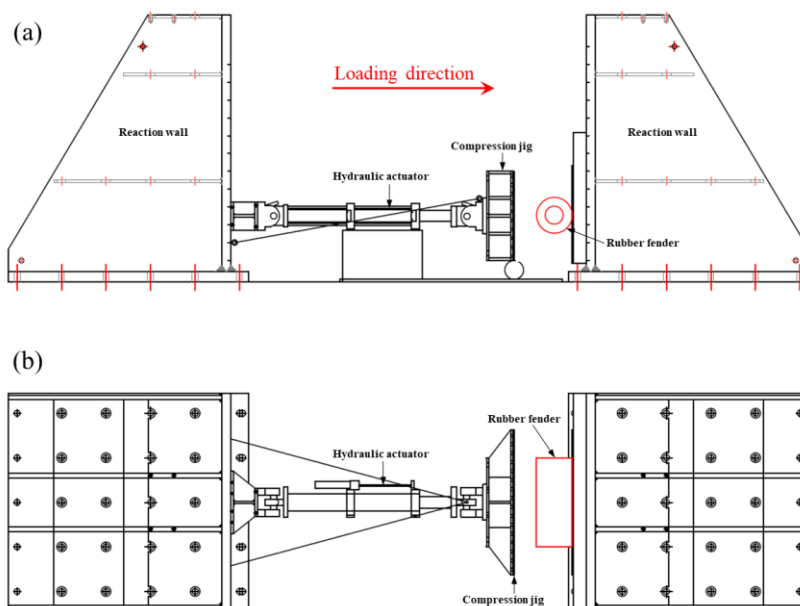

Figure 9. Schematic of test equipment and application direction of loading: (a) Side view, (b) Plan view.

Table 6. Test cases with different test conditions.

Case no.	Load speed (mm/s)	Maximum penetration (mm)	Rest time (s)
1	0.05		-
2	10	200	1,200
3	100		1,200
4	200		1,200
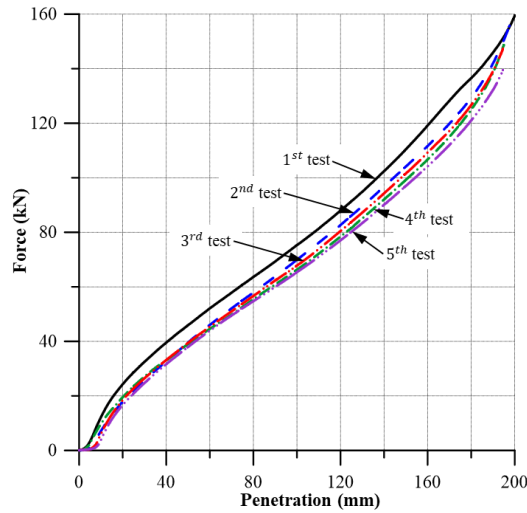
Figure 10. Effect of repeated loading on the crushing behaviour of rubber fender, obtained from the present test at a loading speed of 200 mm/s.

2.3 Computational modelling of solid rubber fender

The solid rubber fender was modelled as an incompressible and hyper-elastic material considering the rubber material properties, using solid eight-node elements. The dimensions of the rubber fender model were modelled comparable those of the test specimen. The reaction wall and compression plate were assumed to be rigid and modelled as shell elements sharing four nodes. The element size was determined to be 25 mm by conducting a convergence study in association with the response (i.e., relation between force and absorbed energy) of the rubber fender, as shown in Figure 11. Figure 12 shows the finite element model of a solid rubber fender to which the previously determined element size is applied.

The constitutive equation of the rubber fender material was defined using the Ogden material model (Ogden 1972), while the tensile test data obtained from the present study was used to determine the coefficients of the Ogden material model. In the LS-DYNA code, the material

10

properties for the rubber fender model were defined using the "MAT 181 Simplified Rubber Model" to consider the dynamic behaviour of the rubber fender. The loading speeds of the compression plate were also varied at 0.05, 10, 100, and 200 mm/s, with the other conditions as the same as in the experiment.
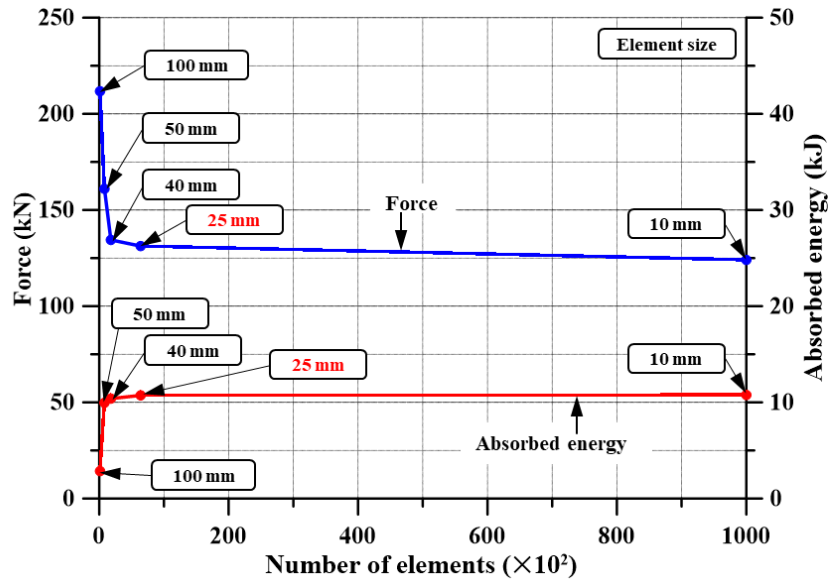

Figure 11. Result of the convergence study to determine the element size of a solid rubber fender.
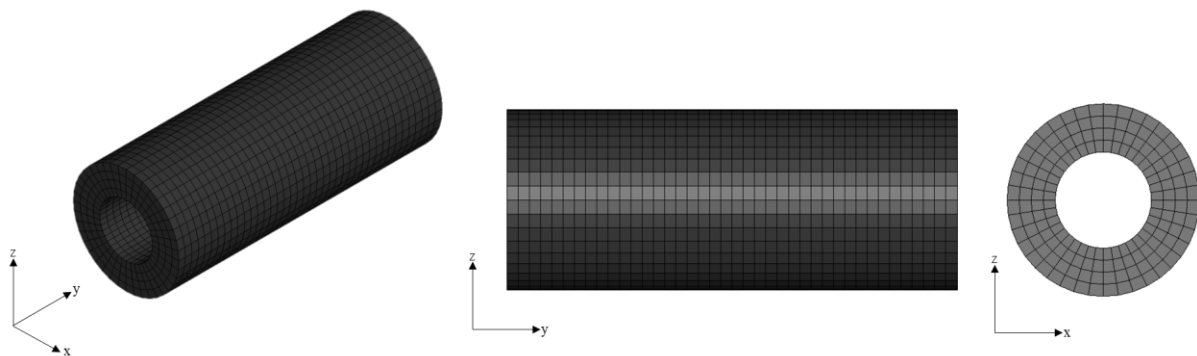

Figure 12. Finite element model of the solid rubber fender used in this study.

2.4 Comparison of physical testing and computational analysis results

Figure 13(a) shows the test data pertaining to the relationship between the force and penetration. The energy absorbed by the rubber fender was defined by integrating the force against penetration, assuming that all the external work energy was used to deform the

11

specimen. Figure 13(b) shows the test data pertaining to the relationship between the absorbed energy and penetration. The force at the dynamic speeds was 15.86% (10 mm/s), 32.28% (100 mm/s), and 32.89% (200 mm/s) higher than that at the quasi-static speed or 0.05 mm/s. Therefore, a higher speed corresponded to smaller increase in the force. The absorbed energy at the dynamic speeds was 21.62% (10 mm/s), 34.16% (100 mm/s), and 40.39% (200 mm/s) higher than that at the quasi-static speed, i.e., the increase rate of the absorbed energy also decreased as the speed increased.

Figure 14 presents the computed data in terms of the force and absorbed energy behaviour of the rubber fender in various speed conditions; all forces were obtained from the compression plate in contact with the rubber fender (as a reaction force). As in the case of the test results, the force and absorbed energy tended to increase as the load speed increased. The force increases rapidly as the number of contact elements increases. The tendency of absorbed energy is almost similar, but the difference in the force between experiment and simulation, specifically in the region of large penetration, is considered to be partly due to the preceding reason, e.g., softening effect of rubber material under repeated loading, as described in section 2.2.

Figure 15 presents a comparison of the energy absorbed by the rubber fender at the same speed conditions in the test and computations. At the rubber fender penetration of 200 mm, the test measurements were -3.56%, 1.33%, 2.51%, and 5.73% higher than the computed value at 0.05 mm/s, 10 mm/s, 100 mm/s and 200 mm/s, respectively. It is of interest to measure strain rates on the collided or contacted areas. Figure 16 shows the variation of strain rates on the contacted area with different loading speeds as the penetration proceeds, which was obtained from the finite element analysis. The strain rates are not constant but vary with penetration. At a loading speed of 200 mm/s, the maximum strain rate is around 12/s.
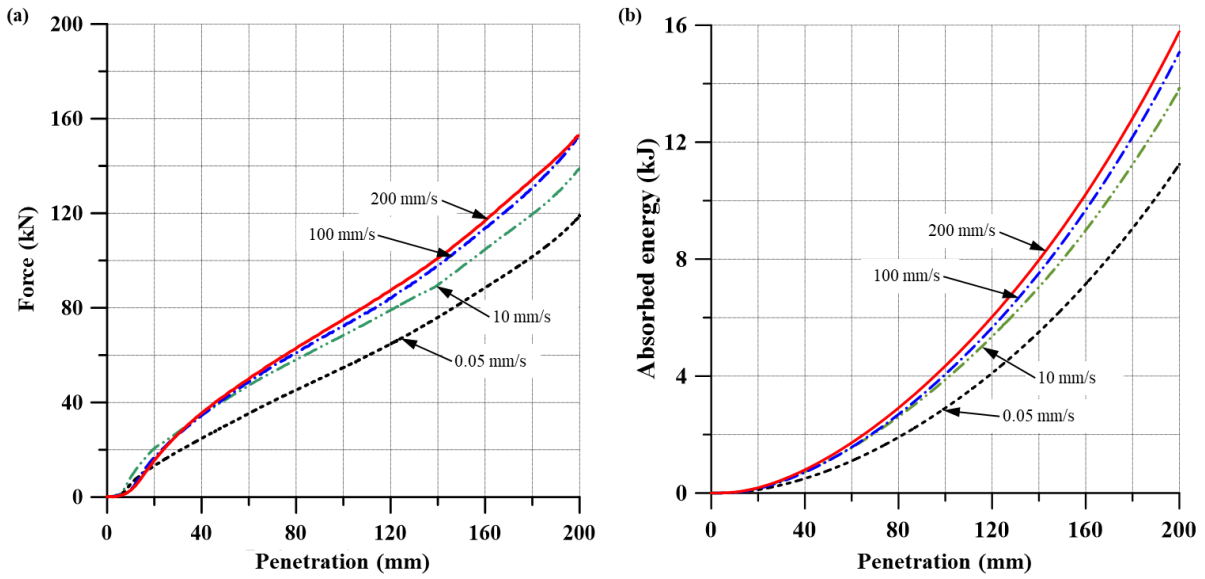
Figure 13. Test result curves at various loading speeds: (a) Relationship between force and penetration, (b) Relationship between absorbed energy and penetration.
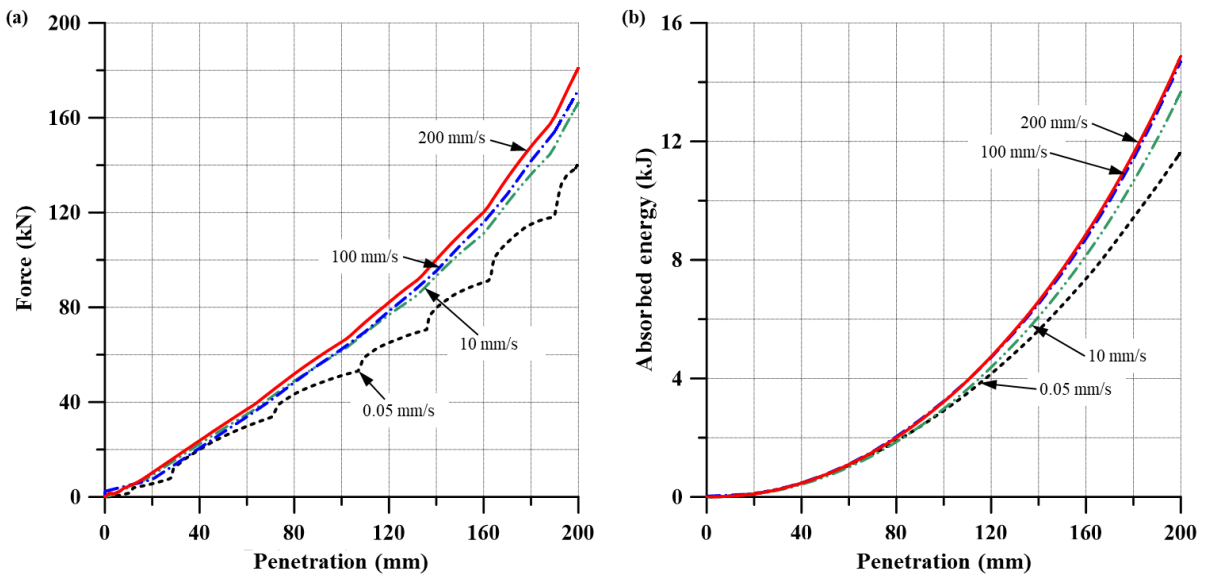

Figure 14. Finite element analysis curves at various loading speeds: (a) Relationship between force and penetration, (b) Relationship between absorbed energy and penetration.
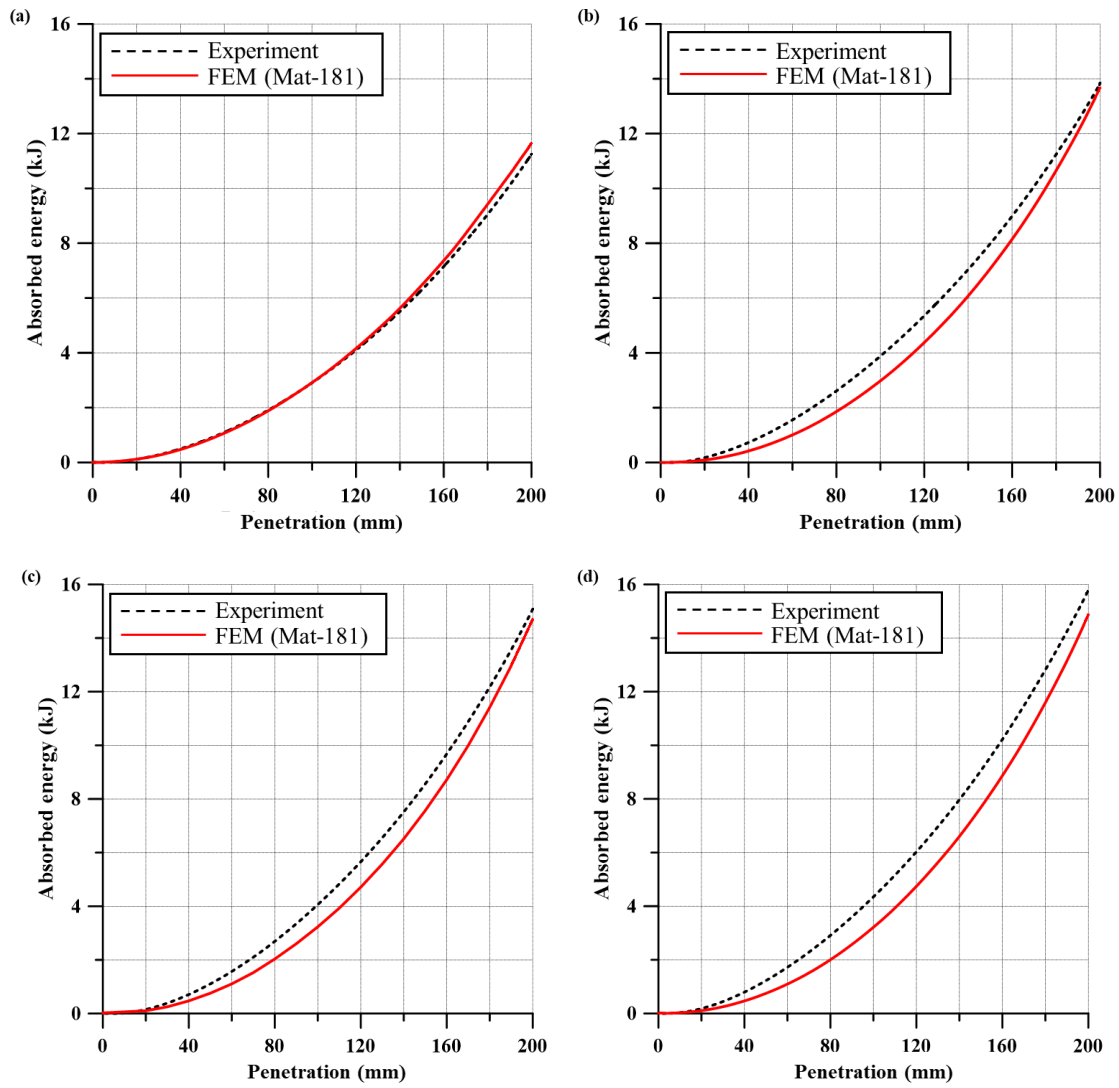
13

Figure 15. Comparison of the finite element analysis and test values at a penetration of 200 mm and loading speed of (a) 0.05 mm/s, (b) 10 mm/s, (c) 100 mm/s, and (d) 200 mm/s.
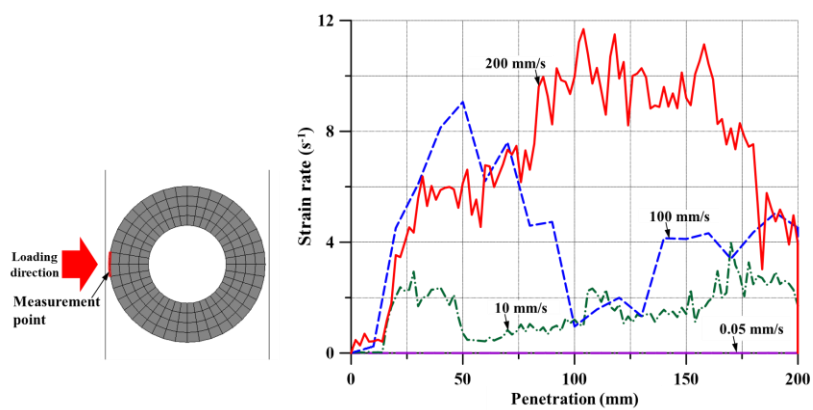

Figure 16. Variation of strain rates on the contacted region with penetration at different loading speeds.

14

3. Crashworthiness of a VLCC class FPSO hull structure that collides with an offshore supply vessel equipped with a solid rubber fender

Case studies were undertaken as indicated in Tables 1 and 2, where the side structure of a very large crude-oil carrier (VLCC) class FPSO unit hull was impacted by the bow structure of a 8,546-ton offshore supply vessel (OSV), both in the full-load condition, as shown in Figure 17. The collision angle between two bodies is 90°.
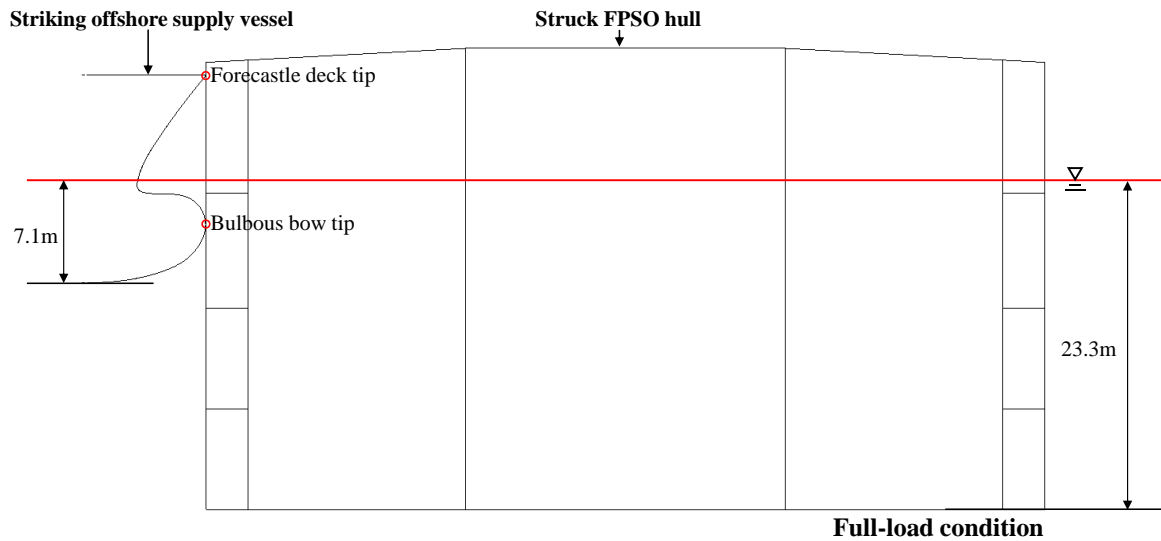

Figure 17. Collision between the bow structures of an OSV and side structures of an FPSO hull in the full-load condition

3.1 Target structure model

The structural crashworthiness was analysed using the LS-DYNA code. In the present study, the struck FPSO was fixed at a standstill condition, and the surrounding water effect (or added mass effect) was not considered.

The struck FPSO was modelled as a ship-shaped offshore installation, corresponding to a VLCC, and Figure 18 shows the finite element model of the FPSO. In the OSV model, only the bow structure section with a high risk of collision impact was modelled, as shown in Figure 19. Specifically, the bow structure section was modelled by applying the total weight at full load to the centre of mass, and Figure 20 shows the distribution of mass through rigid beam elements (Paik 2020, 2022; Mujeeb-Ahmed and Paik 2019, 2021; Mujeeb-Ahmed et al. 2020).

Figure 21 shows the finite element model of the rubber fender, which had an outer diameter of 0.8 m and inner diameter of 0.4 m. Figure 22 shows the rubber fender installed at the OSV, with the fender modelled as a shape surrounding the forecastle deck tip. The computations were performed considering deformable models of the struck ship, striking ship, and rubber fender because computations using a rigid striking ship model are not sufficiently accurate and may be excessively pessimistic in the structural crashworthiness analysis of collisions between ships (Ko et al. 2018a, Paik 2020).
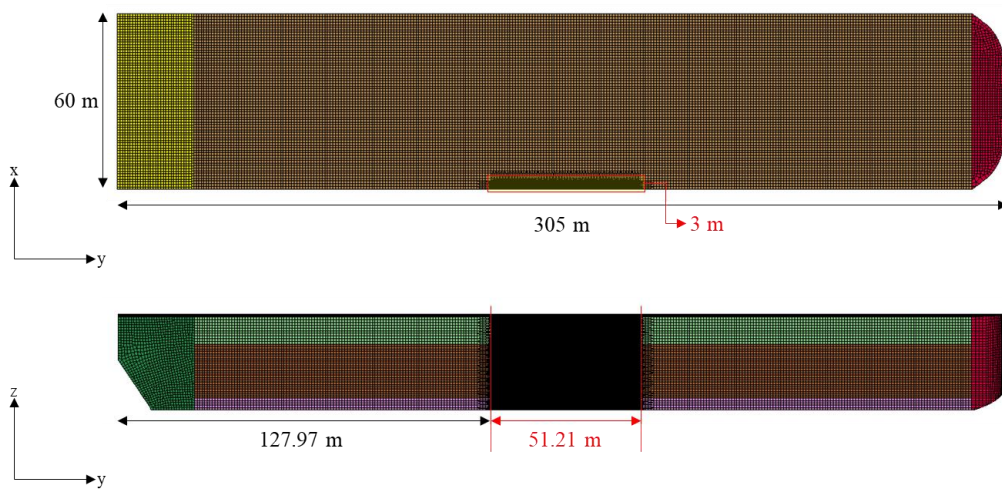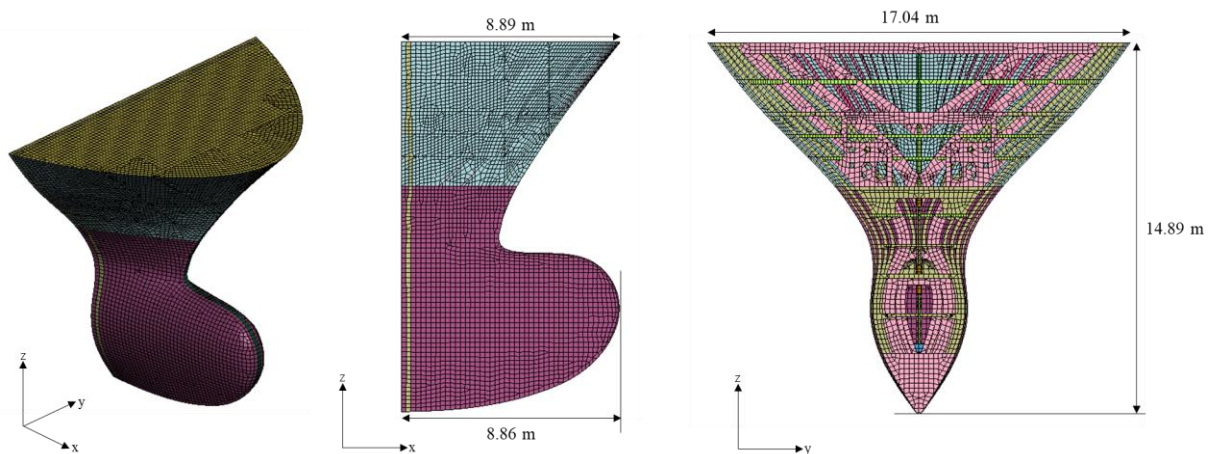

Figure 18. Finite element model of an FPSO hull

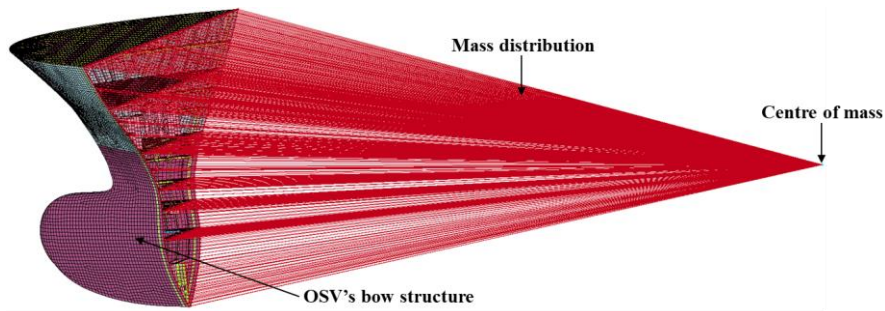Figure 19. Finite element model of the OSV bow structure

Figure 20. OSV full-finite element model with total mass distribution from the centre of mass to the bow structure via a straight-line group.
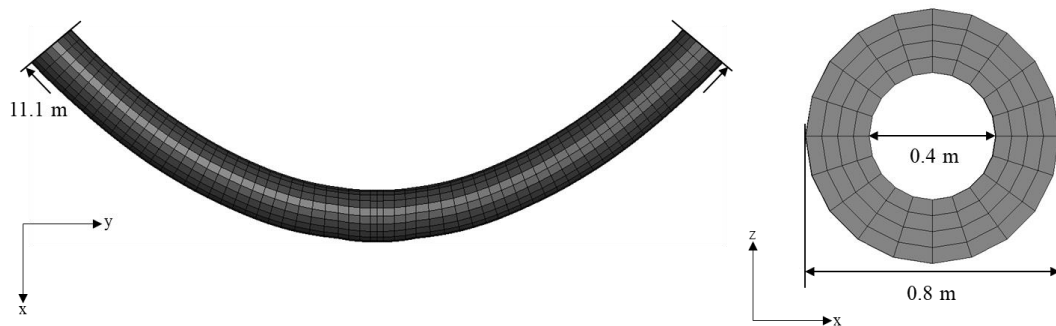

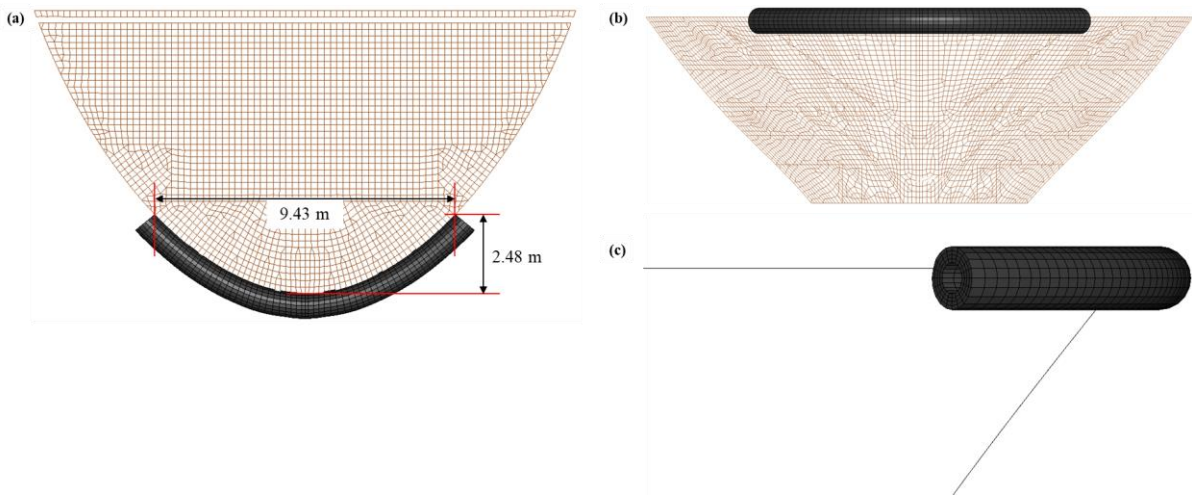Figure 21. Finite element model of the solid rubber fender.

Figure 22. Rubber fender installed on the forecastle deck tip of OSV: (a) Plan view, (b) Section view, (c) Elevation view.

3.2 Type and size of finite elements

The striking ship and struck ship were modelled using shell elements sharing four nodes,

and the rubber fender was modelled using solid elements sharing eight nodes. In general, it is important to determine the appropriate mesh size in FEM modelling because the examination of the structural crashworthiness in ship-to-ship collisions may involve crushing and fracture scenarios (Paik 2020, 2022).

In this study, a coarse mesh, sized 880 mm, was used for shell elements in areas not significantly affected by the collision. In contrast, the shell elements in the area in which the impact of the collision was expected to be high were modelled as a finer mesh. The optimal mesh size for performing the numerical analysis of the structural collision was determined using a simplified method (Paik and Thayamballi 2007; Paik 2007a, 2007b, 2018, 2020, 2022).

Figure 23 shows that at least eight finite elements were required for the half-fold length of the thin plate to describe the crushing behaviour. The mesh size of the finite element that could satisfy this condition was defined using Equation (1) (Paik 2020, 2022).

$$s \leq \frac{H}{8} \tag{1}$$

where s is the element size, and H is the half-fold length of the thin plate, which can be obtained as $H = 0.983 b^{\frac{2}{3}} t^{\frac{1}{3}}$ (Wierzbicki and Abramowicz 1983), where b is the breadth and t is the thickness of the side shell of the FPSO. Substituting this value of H, Equation (1) can be rewritten as follows:

$$s \leq \frac{H}{8} = 0.1228 b^{\frac{2}{3}} t^{\frac{1}{3}} \tag{2}$$

In this study, the structural scantlings of FPSO side structures and the resulting element sizes are given in Table 7, where the element sizes are different for different member locations or scantlings. However, it is not convenient to use different mesh sizes of Table 7 for finite element modelling. Rather, it is more convenient to use the same mesh size regardless of different member locations or scantlings. In this regard, a convergence study was undertaken in terms of the relation between structural response versus mesh size, and the optimal mesh size was determined as 220 mm which is found to be comparable to those of Table 7. Through those series of processes, therefore, the finer mesh size of the shell element was taken as 220 mm. Table 8 summarises the element type and the number of elements in the finite element models of the FPSO, OSV, and rubber fender, determined through the abovementioned series of processes.
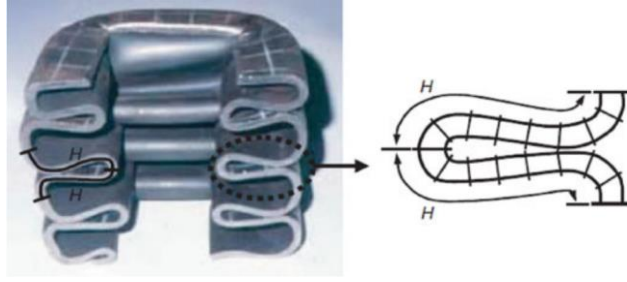
Figure 23. Definition of the half-fold length of crushed thin-walled structure (Paik 2018, 2020, 2022).

Table 7. Element sizes of the FPSO structures, determined from Equation (2).

Structural member feature	Value	
Member location	Web space	Hull depth
Plate breadth, b (mm)	5,690	32,000
Plate thickness, t (mm)	18.0	18.0
Half-fold length, H (mm)	820.6	2595.1
Element size	102.6	324.4

Table 8. Description of elements in the FEM models of the FPSO, OSV, and rubber fender.

Feature		FPSO	OSV	Rubber fender
Element type		Shell	Shell	Solid
Number of fine elements	(220 mm)	143,469	344,347	3,604
Number of coarse elements	(880 mm)	299,002	-	-
Number of total elements		442,471	344,347	3,604

3.3 Material property modelling

For the rubber fender model, the material properties listed in Table 4 and stress–strain curves shown in Figure 5 were applied due to a lack of data tested at a high strain rate. The striking ship was modelled using DH 36 high-tensile steel (Mujeeb-Ahmed et al. 2020), and the struck structure was modelled using mild steel and AH 32 high-tensile steel. The material properties for the high-tensile steel corresponded to the results measured at room temperature (20 °C) in the MPDAS database program (Paik et al. 2017). The yield stress was 281.57 MPa for mild steel and 400.97 MPa for AH 32 high-tensile steel. In addition, the static fracture strains were 0.43 and 0.32 for mild steel and AH 32 high-tensile steel, respectively. The material properties for each ship model are summarised in Table 9 (Paik 2020, 2022).

19

In general, to perform nonlinear FEM analysis of the dynamic fracture behaviour of the model, it is essential to calculate the strain rate and dynamic fracture strain according to the speed. The dynamic yield strength may be determined through Equation (3), known as the Cowper–Symonds equation (Cowper and Symonds 1957; Jones 2012; Paik 2020, 2022):

$$\sigma_{Yd} = \left[1 + \left(\frac{\dot{\varepsilon}}{C} \right)^{\frac{1}{q}} \right] \sigma_Y \tag{3}$$

where σ_Y and σ_{Yd} are the static and dynamic yield stresses, respectively, $\dot{\varepsilon}$ is the strain rate, and C and q are the Cowper–Symonds coefficients, specified in Table 8. The strain rate with respect to the initial collision speed was estimated using Equation (4) (Ko et al. 2018a; Paik 2020).

$$\dot{\varepsilon} = 2.970 V_0 - 0.686 \text{ for } V_0 \geq 0.231 m / s \tag{4}$$

where V_0 is the collision speed (in m/s) of the striking ship. The dynamic fracture strain of the material is defined as the inverse of the Cowper–Symonds equation, as in Equation (5) (Paik et al. 2017; Ko et al. 2018b; Paik 2018, 2020).

$$\varepsilon_{fd} = \left[1 + \left(\frac{\dot{\varepsilon}}{C} \right)^{\frac{1}{q}} \right]^{-1} \varepsilon_{fc} \tag{5}$$

where ε_{fd} and ε_{fc} are the dynamic fracture strain and critical fracture strain, respectively. ε_{fc} is defined as in Equation (6) (Paik 2007a, 2007b, 2018, 2020).

$$\varepsilon_{fc} = \gamma d_1 \left(\frac{t}{s} \right)^{d_2} \varepsilon_f \tag{6}$$

where ε_f is the static fracture strain obtained from the testing database; t is the thickness of the plate, set as 17 mm or 20mm; and s is the mesh size, set as 220 mm; and γ is the correction (knock-down) factor, which is taken as 0.3 in Equation (6); and d_1, d_2 are coefficients. For carbon steel with a thickness of 2 mm at room temperature, d_1, d_2 are 4.1, 0.58, respectively (Paik and Thayamballi 2007). Table 10 lists the material properties corresponding to the

dynamic behaviour at each collision speed, defined through the abovementioned series of equations.

Table 9. Material properties of the OSV and FPSO structures.

FPSO features	Description		OSV features	Description
Material	Mild steel	AH32	Material	DH36
Density (kg/m^3)	7850	7850	Density (kg/m^3)	7850
Modulus of elasticity (GPa)	205.8	205.8	Modulus of elasticity (GPa)	205.8
Poisson's ratio	0.3	0.3	Poisson's ratio	0.3
Yield stress (MPa)	281.57	400.97	Yield stress (MPa)	380
Coefficient of friction	0.3	0.3	Coefficient of friction	0.3
Cowper–Symonds coefficients, C (1/s)	40.4	3200	Cowper–Symonds coefficients, C (1/s)	3200
Cowper–Symonds coefficients, q	5	5	Cowper–Symonds coefficients, q	5

Table 10. Dynamic fracture strains used for the FEM analysis.

Steel grade	Collision speed (m/s)	Yield stress (MPa)	Strain rate (1/s)	Static fracture strain	Critical fracture strain	Dynamic fracture strain
Mild steel	1.03	281.57	2.37	0.429	0.120	0.076
	2.06		5.43			0.072
	3.09		8.48			0.069
	4.12		11.54			0.067
HT steel (AH32)	1.03	400.97	2.37	0.324	0.099	0.080
	2.06		5.43			0.078
	3.09		8.48			0.076
	4.12		11.54			0.075

3.4 Results and discussions

A total of eight study cases (Table 2) were considered in the LS-DYNA nonlinear FEM analyses. First, the resultant force–time, penetration–time, and absorbed energy–time relationships were obtained from the computational results. The resultant force versus penetration curves were derived from the computation results in which the resultant force and penetration were determined simultaneously. In the LS-DYNA simulations, the absorbed energies were automatically computed in terms of strain energies, which were calculated as a function of stresses and strains in the elements.

The maximum penetration is a primary parameter when the bow structure of a striking ship penetrates the side structure of a struck ship (Ko et al. 2018; Paik 2020, 2022). In this study, the penetration was measured at the tip of the forecastle deck and bulbous bow of the striking ship, which corresponded to the maximum sideways penetration of the struck vessel members by the striking OSV members in the centre position of the struck FPSO. According to Paik and Pederson (1995), the resultant forces between the striking and struck ships must be in equilibrium.

Figure 24 shows the relationship between the resultant force and time during penetration at various speeds. Figures 24 (a) and 24 (b) show the scenarios in which the striking ship without and with a rubber fender collided with the struck ship, respectively. Figure 25 presents the deformed shapes of the striking and struck ships at speeds of 2 kt, 4 kt, 6 kt, and 8 kt at maximum penetration in the presence and absence of the rubber fenders. Figure 26 indicates the relationship between the maximum penetration and collision speed. The amount of damage and extension were generally higher when the striking ship without rubber fenders collided with the side structures of the struck ship than those in the case in which rubber fenders were installed. Figure 26 shows that the differences of penetration cases with and without fender at different collision speeds are 9.76% for 2 kt, -6.98% for 4 kt, 75.11% for 6 kt, and 80.88% for 8 kt in the flare deck tip of the striking ship, or 10.53% for 2 kt, 12.50% for 4 kt, 14.34% for 6 kt, and 6.08% for 8 kt in the bulbous bow tip of the striking ship.

As shown in Figure 26 (a), the maximum penetration in the forecastle deck tip when the rubber fender was installed was significantly lower than that when the rubber fender was not installed because the forecastle deck tip of the striking ship became blunt when the rubber fender was installed at the bow structure of the striking ship. Figures 27 and 28 present the deformed shape of the side and inner side structures of the struck ship owing to the striking ship, respectively. The advantage of installing the rubber fender was evident in terms of not only the maximum penetration but also the magnitude of the damage to the hull struck by the striking ship.

Table 11 summarises the initial kinetic energy and absorbed energy at the striking ship, struck ship, and rubber fender until all of the kinetic energy was consumed at maximum penetration. When the striking OSV was equipped with a rubber fender, the contribution to the energy absorption by the struck vessel was decreased by 29.76%, 5.65%, 35.38%, and 30.21% at a collision speed of 2, 4, 6, and 8 kt, respectively. The reason why the trend of contributing

energy absorption by the struck vessel is not continuous is that the contacted area becomes different depending on the collision scenarios. However, it is obvious that the energy absorbed by the struck vessel colliding with a striking OSV equipped with a rubber fender was lower than that in the case without the fender up to a collision speed of 8 kt (4.12 m/s), i.e., the struck ship absorbed less energy when the striking OSV had a fender. This has implications for structural crashworthiness. Figures A.1 and A.2 in the Appendix present details of the LS-DYNA computational results.

It is of interest to measure the strain rate levels at the impacted areas. Figure 29 shows the (maximum) strain rates at the impacted areas with penetration of the striking OSV. Figure 29(a) specifies the strain rates of rubber fender with different collision speeds, and Figure 29(b) specifies the strain rates of bulbous bow with different collision speeds. It is observed that the maximum strain rate at the forecastle deck tip reaches 100/s at a collision speed of 8 kt.

The present study has numerically performed a series of collision simulations between ships in consideration of fracture behaviour with varying initial speeds of the striking ship. While the collision simulations are ongoing, the eroded mesh occurred and it led to energy losses within the entire system. The present study focused on the prevention of structural damage due to collision with the forecastle deck tip of the striking OSV equipped with solid rubber fender, but it is obvious that the bulbous bow impact can cause significant damage and thus further study is recommended to resolve this issue.
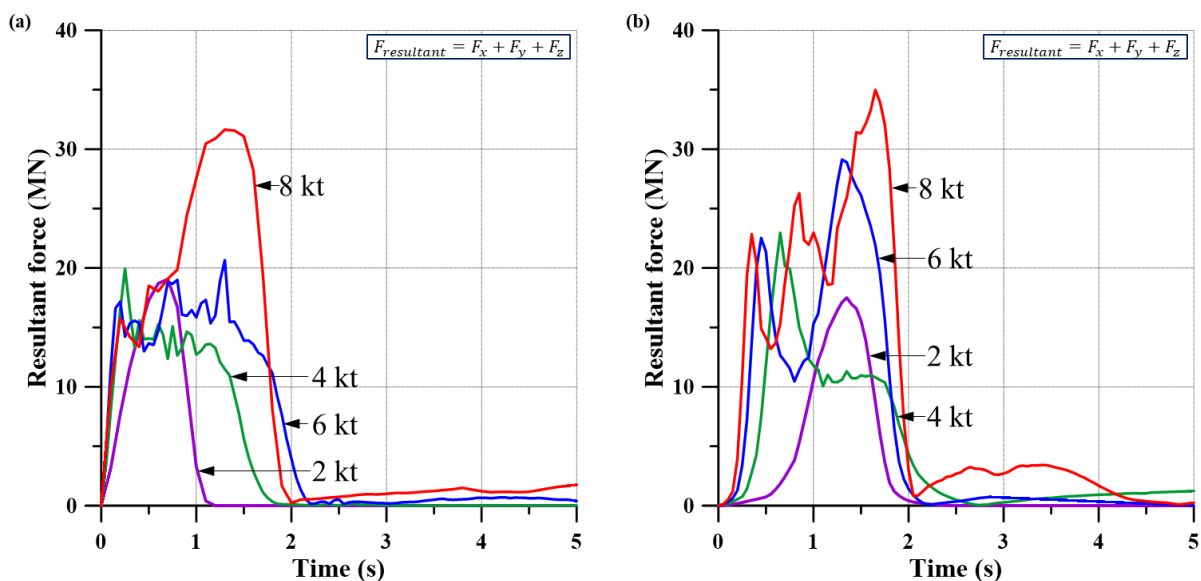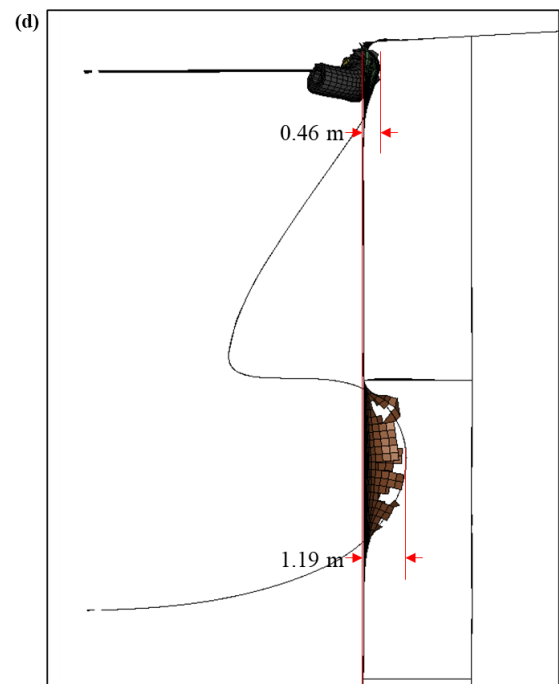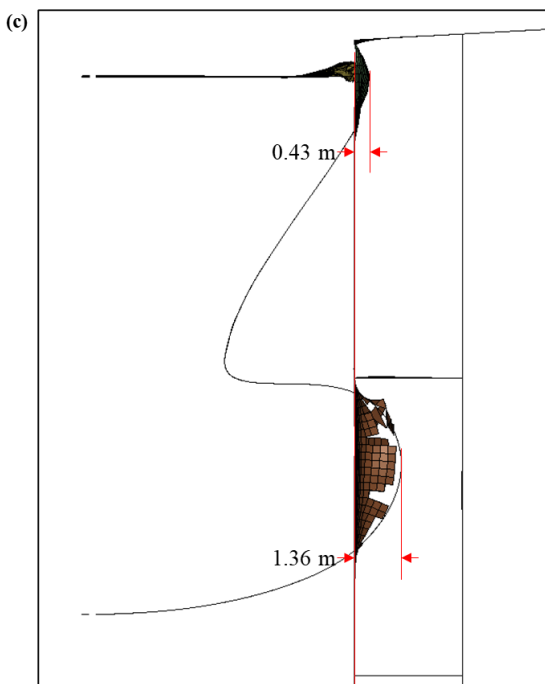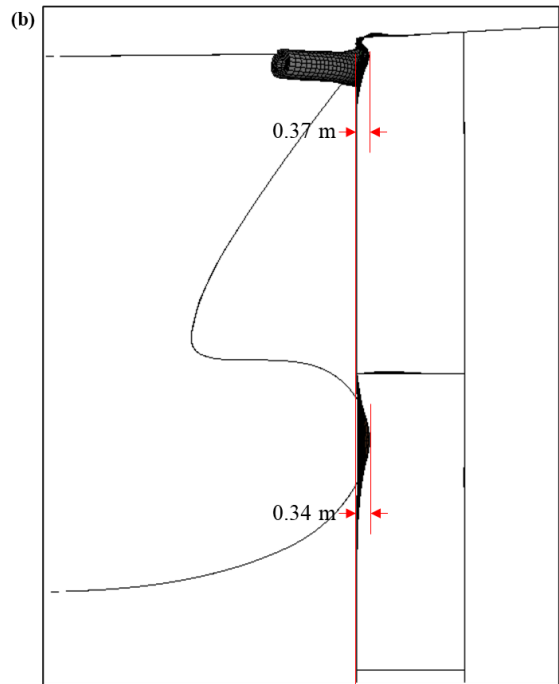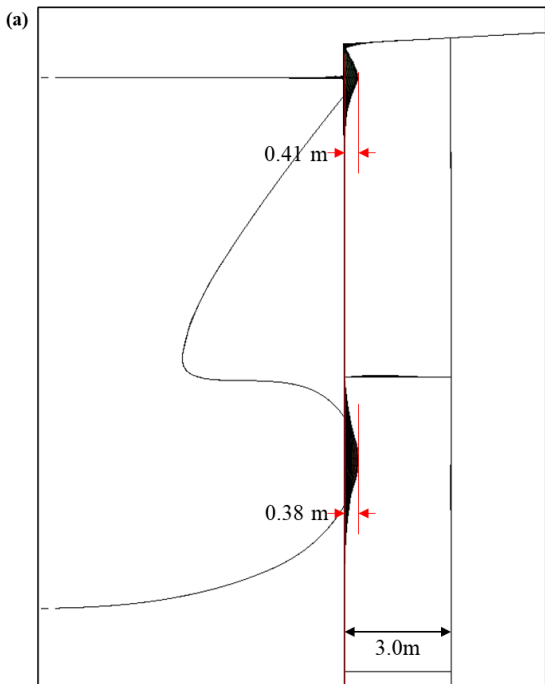

Figure 24. Resultant force–time relation curve for collision between striking OSV and struck FPSO at several velocities: (a) Striking ship without rubber fender, (b) Striking ship with

rubber fender.

(a)

0.41 m

0.38 m

3.0m

(b)

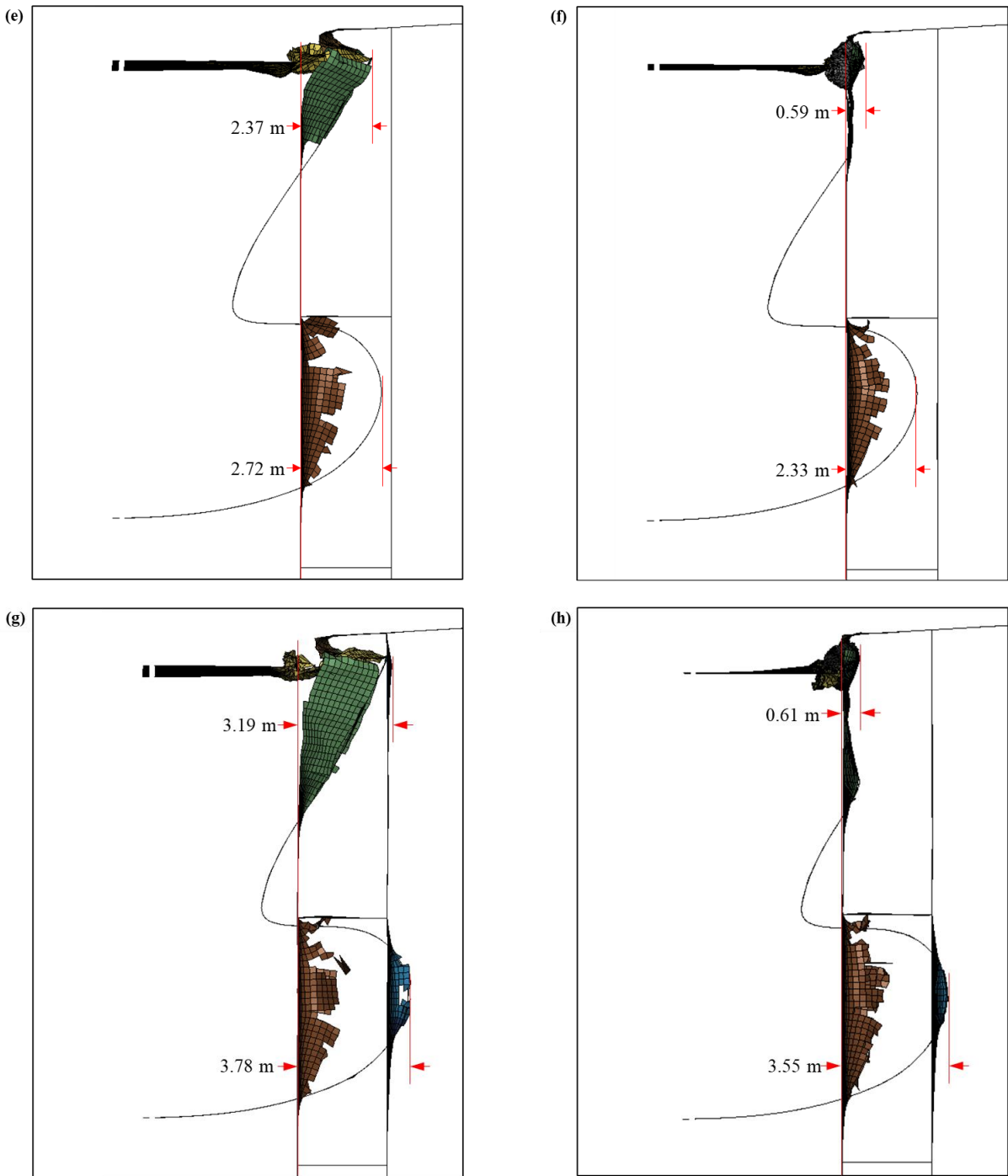0.37 m

0.34 m

(c)

0.43 m

1.36 m

(d)

0.46 m

1.19 m

Figure 25. Maximum penetration of the flare deck tip and bulbous bow tip of the OSV at different velocities in the presence and absence of a rubber fender: Scenarios with a collision speed of 2 kt (a) without and (b) with the rubber fender, 4 kt (c) without and (d) with the rubber fender, 6 kt (e) without and (f) with the rubber fender, 8 kt (g) without and (h) with the rubber fender.
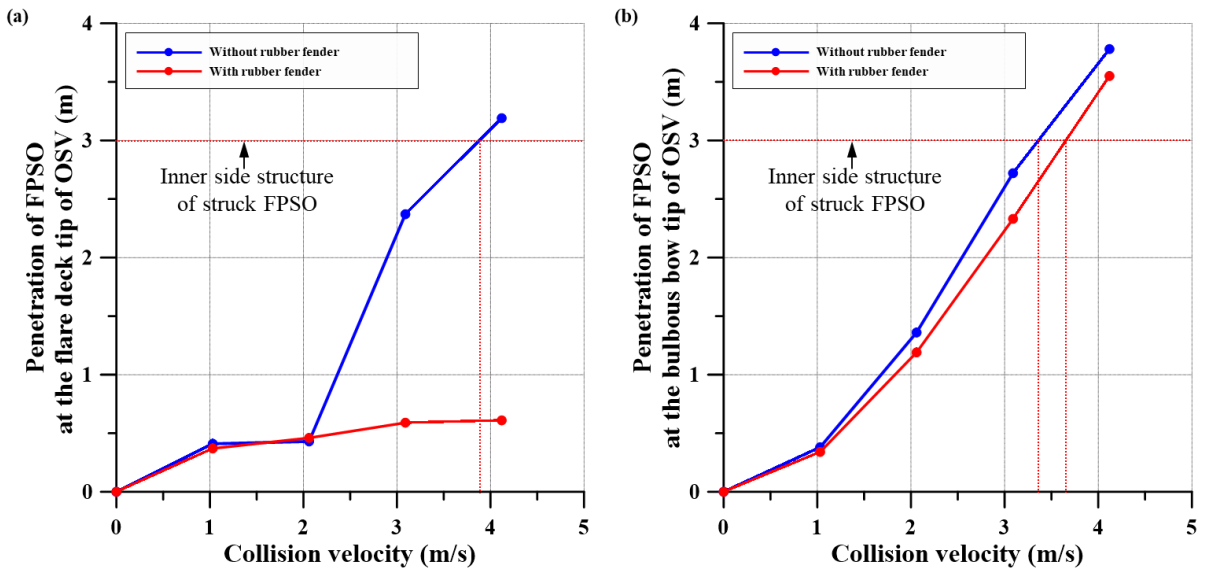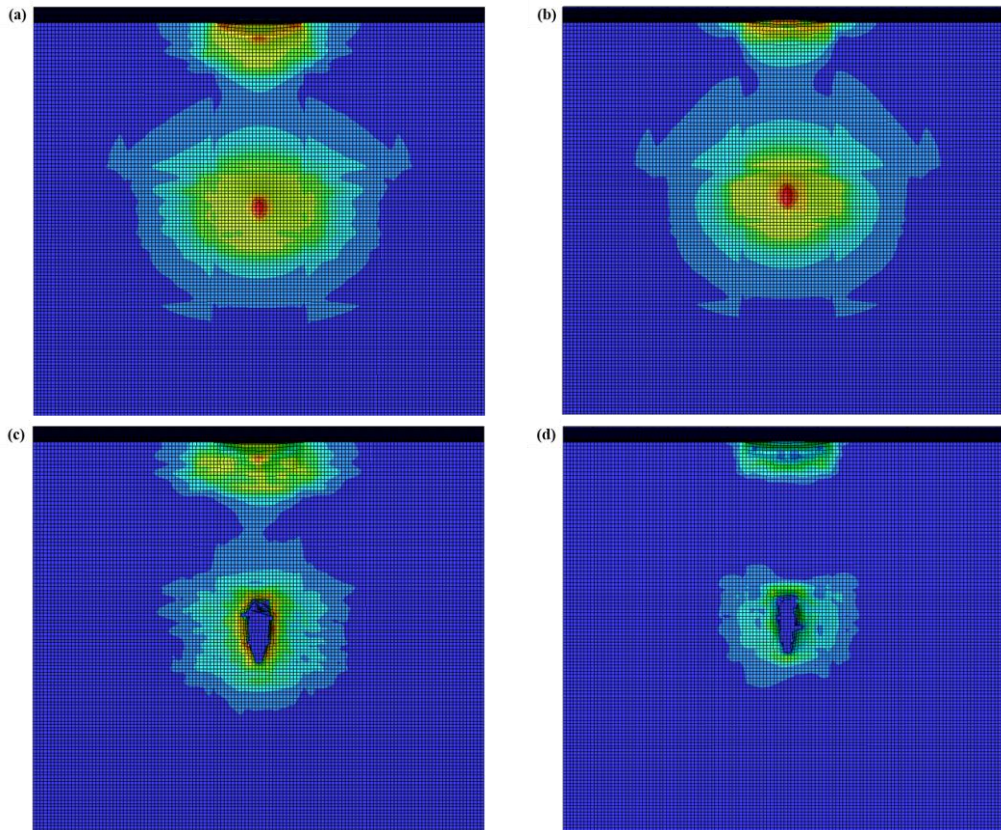
Figure 26. Maximum penetration–collision speed relation curves for the side structure of the struck FPSO in the collision between an FPSO and an OSV with and without a rubber fender. Penetration at the tip of the (a) forecastle deck and (b) bulbous bow of the striking ship.
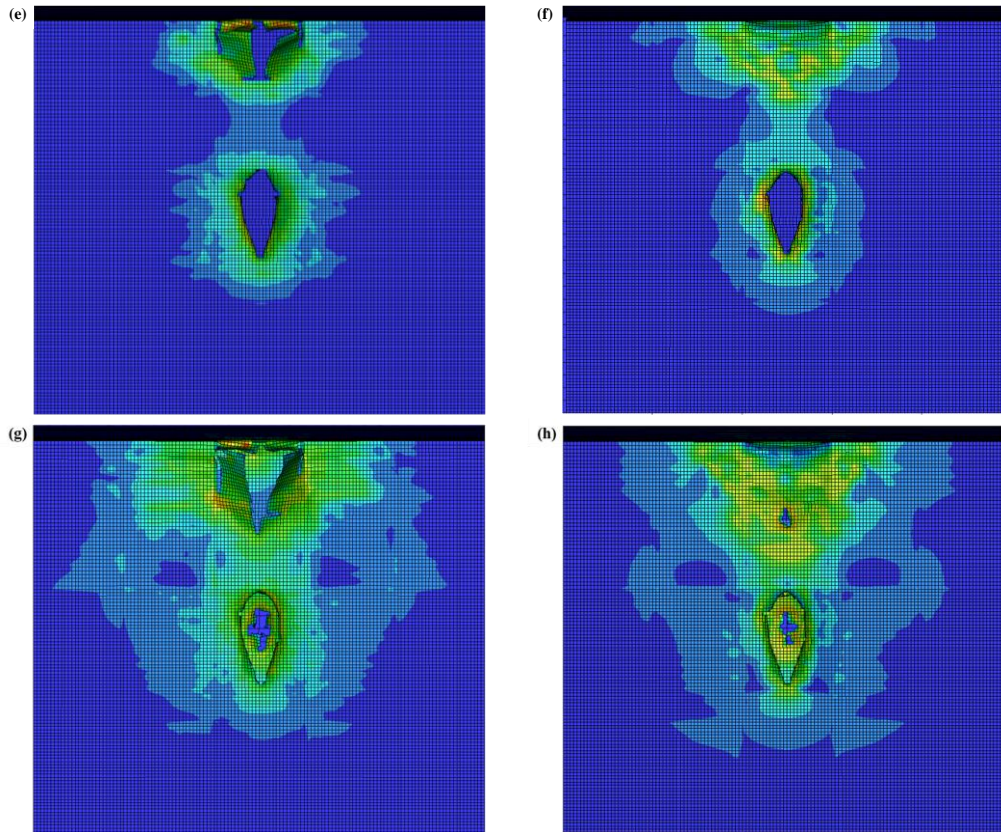

26

Figure 27. Deformed shapes of the FPSO side structures struck by the OSV bulbous bow structure at different collision velocities in the presence and absence of the rubber fender: Scenarios with a collision speed of 2 kt (a) without and (b) with the rubber fender, 4 kt (c) without and (d) with the rubber fender, 6 kt (e) without and (f) with the rubber fender, 8 kt (g) without and (h) with the rubber fender.
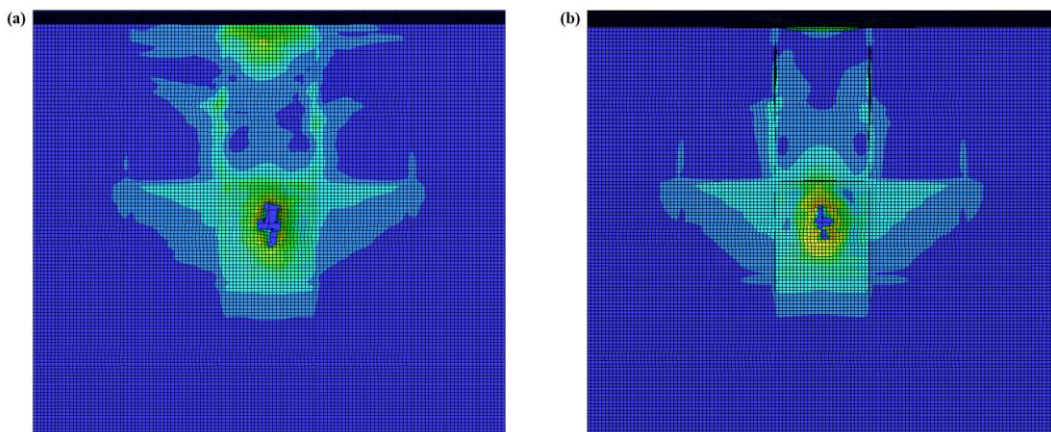

Figure 28. Deformed shapes of the FPSO inner side structures struck by the OSV bulbous bow structure at a collision speed of 8 kt (a) without and (b) with the rubber fender.

Table 11. Absorbed energy before the kinetic energy is entirely consumed

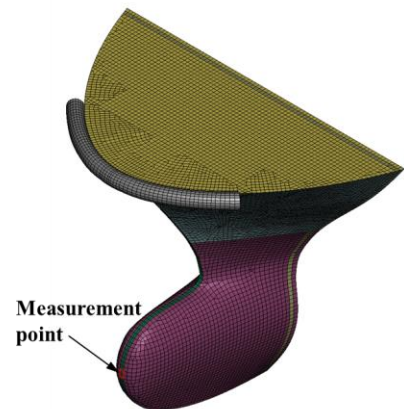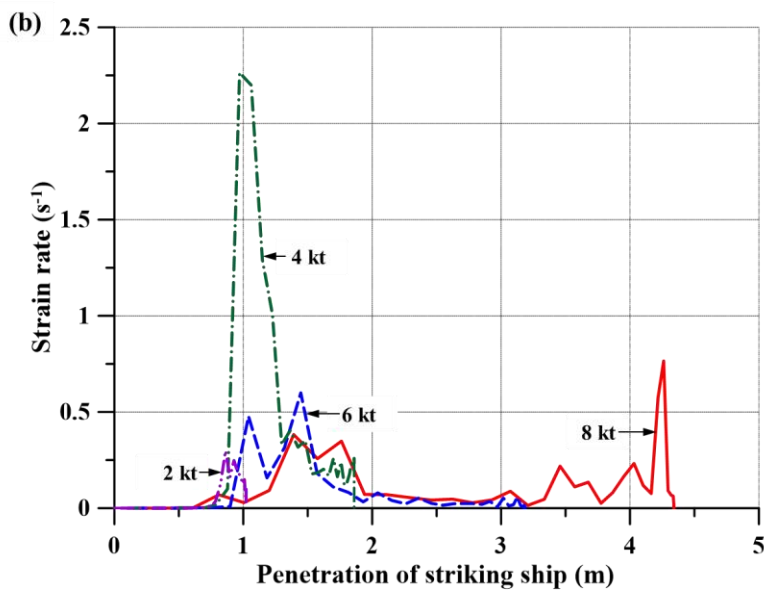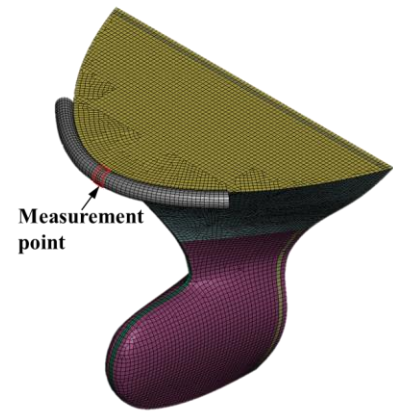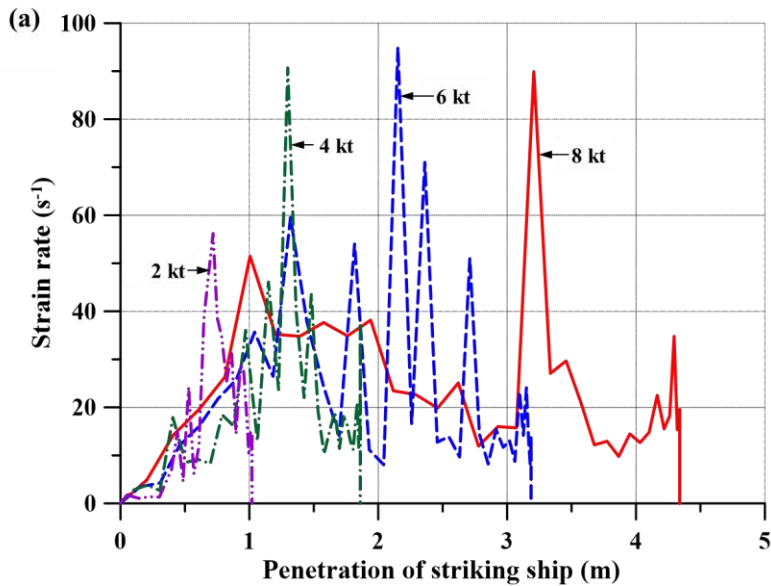| Case no.	Initial kinetic energy (MJ)	Absorbed energy (MJ)			
		Total	Struck FPSO	Striking OSV	Rubber fender
1	4.52	4.34	4.10	0.24	Not installed
2	4.52	3.86	2.88	0.07	0.92
3	18.10	15.29	9.02	6.27	Not installed
4	18.10	14.94	8.51	4.50	1.92
5	40.71	31.61	20.32	11.29	Not installed
6	40.71	32.29	13.13	16.30	2.86
7	72.38	55.28	32.47	23.05	Not installed
8	72.38	57.35	22.66	31.82	2.88

28

Figure 29. Maximum strain rates at impacted areas with penetration of the striking OSV.

4. Concluding remarks

This study evaluated the structural crashworthiness performance during collisions between a ship-shaped offshore installation and an OSV equipped with solid rubber fenders.

Physical crushing model testing was performed and the corresponding computational model was developed to incorporate the rubber fender in the nonlinear FEM computations. The physical crushing model testing of the rubber fender was conducted at the ICASS/KOSORI test site in Hadong, South Korea (www.icass.center).

The numerical analysis of rubber fenders was implemented in the LS-DYNA nonlinear FEM analysis program, with the conditions being identical to those in the physical model test. The material properties of the rubber fender corresponded to the nominal stress–nominal strain curves measured at speeds of 0.01/s, 1/s, 10/s, and 100/s, and the rubber material properties were set using the "MAT 181 Simplified Rubber model" of LS-DYNA code.

Nonlinear FEM computations for eight collision scenarios were performed using the LS-DYNA nonlinear FEM analysis program to examine the structural crashworthiness. The struck ship was a VLCC-class hypothetical FPSO, assumed to be a ship-shaped offshore installation, and the striking ship was an OSV with or without rubber fenders. The collision angle was set as 90° between the web-web form of both sides based on the midship section of the struck ship, and the collision speeds were varied at 2, 4, 6, and 8 kt. Both the struck ship and the striking ship were considered to be at full load and modelled as deformable bodies with material properties considering the dynamic effect. The rubber fender for ships, which is generally a cylindrical solid, was modelled as a deformable body and subjected to the developed modelling technique. The following conclusions were derived:

1. In the physical crushing model test, the kinetic energy absorption performance of the rubber fender was investigated. The force and kinetic energy absorption performance of the rubber fender increased as the load speed (or strain rate) increased. When the deformation of the rubber fender was 200 mm/s, the force and absorbed energy at the maximum speed were 32.89% and 40.39% higher, respectively, than those at the quasi-static condition (or a loading speed of 3 mm/min).

2. The difference in the kinetic energy absorption performance between the physical model

and the numerical analysis with the computational model was 1.33–5.73%. The difference in the structural crashworthiness between them increased as the collision speed increased causing larger deformations. It is considered that such differences are partly due to the softening effect of rubber material under repeated loading, which was not taken into account in the computation model, while a series of testing at different loading speeds were undertaken repeatedly with the same fender model.

3. When the rubber fender was installed on the forecastle deck tip of the striking ship, the resulting penetration at the forecastle deck tip and bulbous bow tip of the striking ship was 80.88% and 14.34% lower than that without the fenders, respectively.

4. When the striking ship was equipped with a rubber fender, the absorbed energy of the struck ship decreased by 30.21% at a collision speed of 8 kt.

5. The presence of a rubber fender considerably improved the structural crashworthiness of a struck ship in terms of the degree of damage and resulting penetration.

6. The proposed approach can facilitate the quantitative evaluation of the structural crashworthiness in ship-to-ship collision scenarios with rubber material protection. In addition, the findings can provide reference in the design of ships equipped with rubber fenders.

7. The present study focused on the collision damage by the forecastle deck tip equipped with solid rubber fender, but the bulbous bow of a striking OSV can cause significant collision damage and thus further study is recommended to resolve this issue.

References

Bondy M. 2013. Development of procedures for accurate finite element modeling of the dynamic and quasi-static performance of automotive chassis components incorporating hyperelastic materials [PhD thesis]. University of Windsor: Electronic Theses and

Dissertations. 4757.

Cowper GR, Symonds PS. 1957. Strain-hardening and strain-rate effects in the impact loading of cantilever beams. Providence (RI): Division of Applied Mathematics, Brown University. Technical Report No. 28.

Fan W, Zhang Z, Huang X, Sun W. 2020. A simplified method to efficiently design steel fenders subjected to vessel head-on collisions. Mar. Struct. 74: 102840.

Fernandez JM, Vaz MA, Cyrino JC. 2021. Numerical study on the collision of platform supply vessel and floating production storage and offloading platform. Ships Offshore Struct. 1-13.

Jones N. 2012. Structural impact. Second Edition, Cambridge, UK: Cambridge University Press.

Ko YG, Kim SJ, Paik JK. 2018a. Effects of a deformable striking ship's bow on the structural crashworthiness in ship–ship collisions. Ships Offshore Struct. 13(sup1). 228-250.

Ko YG, Kim SJ, Sohn JM, Paik JK. 2018b. A practical method to determine the dynamic fracture strain for the nonlinear finite element analysis of structural crashworthiness in ship–ship collisions. Ships Offshore Struct. 13(4). 412-422.

Mujeeb-Ahmed MP, Ince ST, Paik JK. 2020. Computational models for the structural crashworthiness analysis of a fixed-type offshore platform in collisions with an offshore supply vessel. Thin-Walled Struct. 154: 106868.

Mujeeb-Ahmed MP, Paik JK. 2019. A probabilistic approach to determine design loads for collision between an offshore supply vessel and offshore installations. Ocean Eng. 173. 358-374.

Mujeeb-Ahmed MP, Paik JK. 2021. Quantitative collision risk assessment of a fixed-type offshore platform with an offshore supply vessel. Structures. 29. 2139-2161.

Mullins L. 1969. Softening of rubber by deformation. Rubber Chem. Technol. 42(1). 339-362.

Ogden RW. 1972. Large deformation isotropic elasticity–on the correlation of theory and experiment for incompressible rubberlike solids. Proc. R. Soc. A. 326(1567). 565-584.

Ozguc O. 2020a. Numerical assessment of FPSO platform behaviour in ship collision. Trans. Marit. Sci. 9(02). 161-186.

Ozguc O. 2020b. Collision damage analysis of FPSO hull caisson protection structure. Trans. Marit. Sci. 9(02). 130-149.

Paik JK. 2007a. Practical techniques for finite element modeling to simulate structural crashworthiness in ship collisions and grounding (Part I: Theory). Ships Offshore Struct. 2(1). 69-80.

Paik JK. 2007b. Practical techniques for finite element modeling to simulate structural crashworthiness in ship collisions and grounding (Part II: Verification). Ships Offshore Struct. 2(1). 61-86.

Paik JK. 2018. Ultimate limit state analysis and design of plated structures. Second Edition, Chichester, UK: John Wiley &Sons.

Paik JK. 2020. Advanced structural safety study: with extreme conditions and accidents. Singapore: Springer.

Paik JK. 2022. Ship-shaped offshore installations: Design, construction, operation, healthcare and decommissioning. Second Edition, Cambridge, UK: Cambridge University Press.

Paik JK, Kim KJ, Lee JH, Jung BG, Kim SJ. 2017. Test database of the mechanical properties of mild, high-tensile and stainless steel and aluminium alloy associated with cold temperatures and strain rates. Ships Offshore Struct. 12(sup1). S230-S256.

Paik JK, Pedersen PT. 1995. On design of double hull tankers against collisions. Proceedings of 6th International Symposium on Practical Design of Ships and Mobile Units; 17-22 Sept; Seoul, Korea.

Paik JK, Thayamballi AK. 2007. Ship-shaped offshore installation: design, building, and operation. Cambridge: Cambridge University Press.

Park SM, Kim HJ, Cho HR, Kong KH, Park DK, Paik JK. 2022. Effect of pneumatic rubber fenders on the prevention of structural damage during collisions between a ship-shaped offshore installation and a shuttle tanker working side-by-side. Ships and Offshore Structures. doi.org/10.1080/17445302.2022.2085898.

Pedersen PT, Zhang S. 1998. On impact mechanics in ship collisions. Mar. Structures. 11. 429-449.

PIANC. 2002. MarCom WG 33: Guidelines for the design of fender system (2002-2004). Report of Working Group 33 of the Maritime Navigation Commission, The World Association for Waterborne Transport Infrastructure, Brussels.

Wierzbicki T, Abramowicz W. 1983. On the crushing mechanics of thin-walled structures. J. Appl. Mech. 50(4a). 727-734.

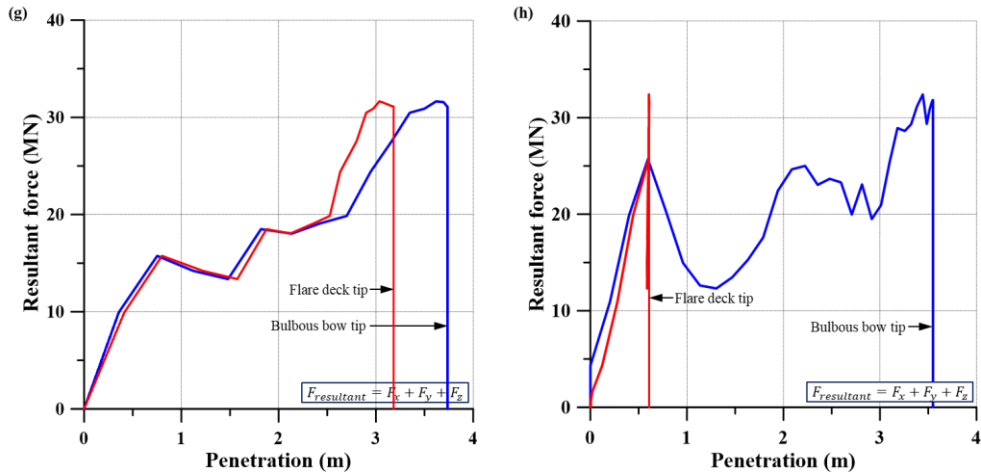# Appendix: LS-DYNA computations of the structural crashworthiness
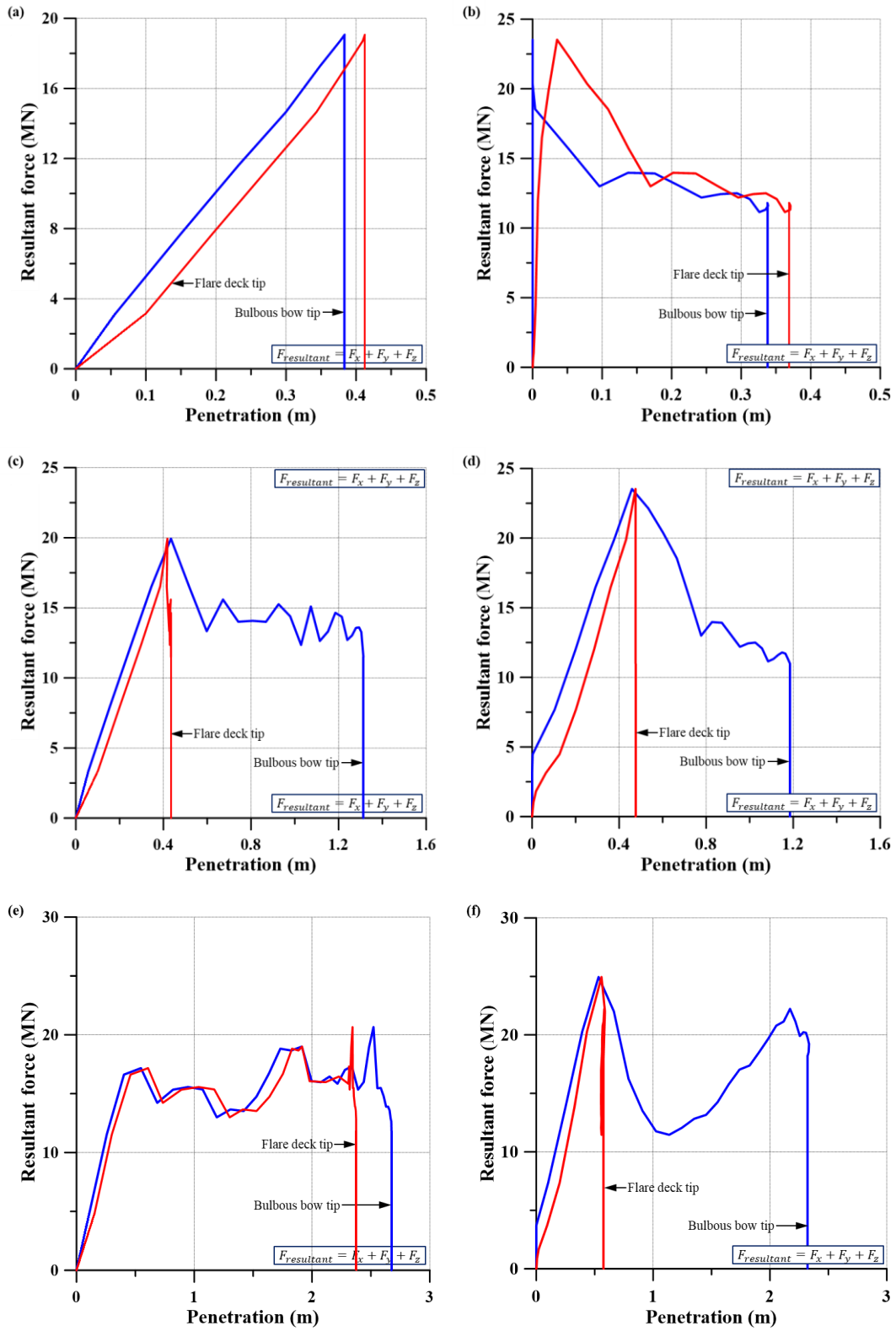
Figure A.1. Relationships between the resultant force and penetration at the tip of forecastle deck and bulbous bow of the striking ship at different collision speeds in the presence and absence of a rubber fender: Scenarios with a collision speed of 2 kt (a) without and (b) with the rubber fender, 4 kt (c) without and (d) with the rubber fendr,; 6 kt (e) without and (f) with the rubber fender, 8 kt (g) without and (h) with the rubber fender.
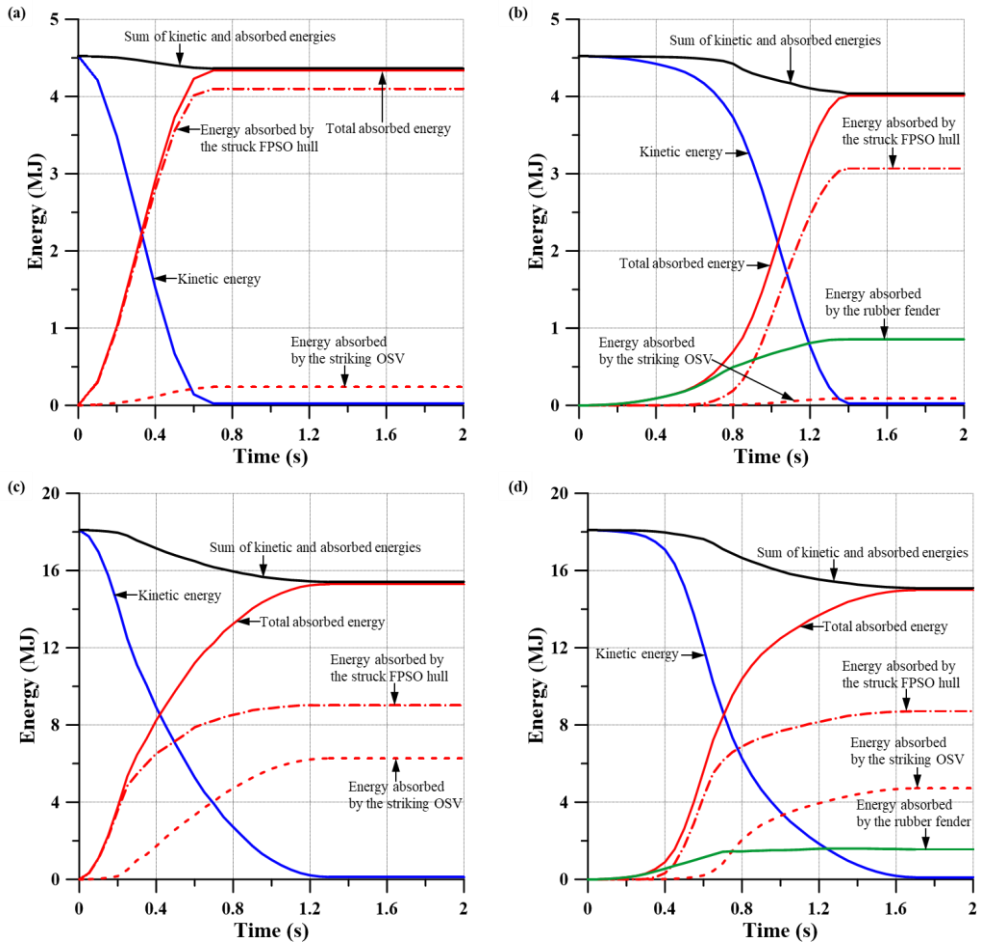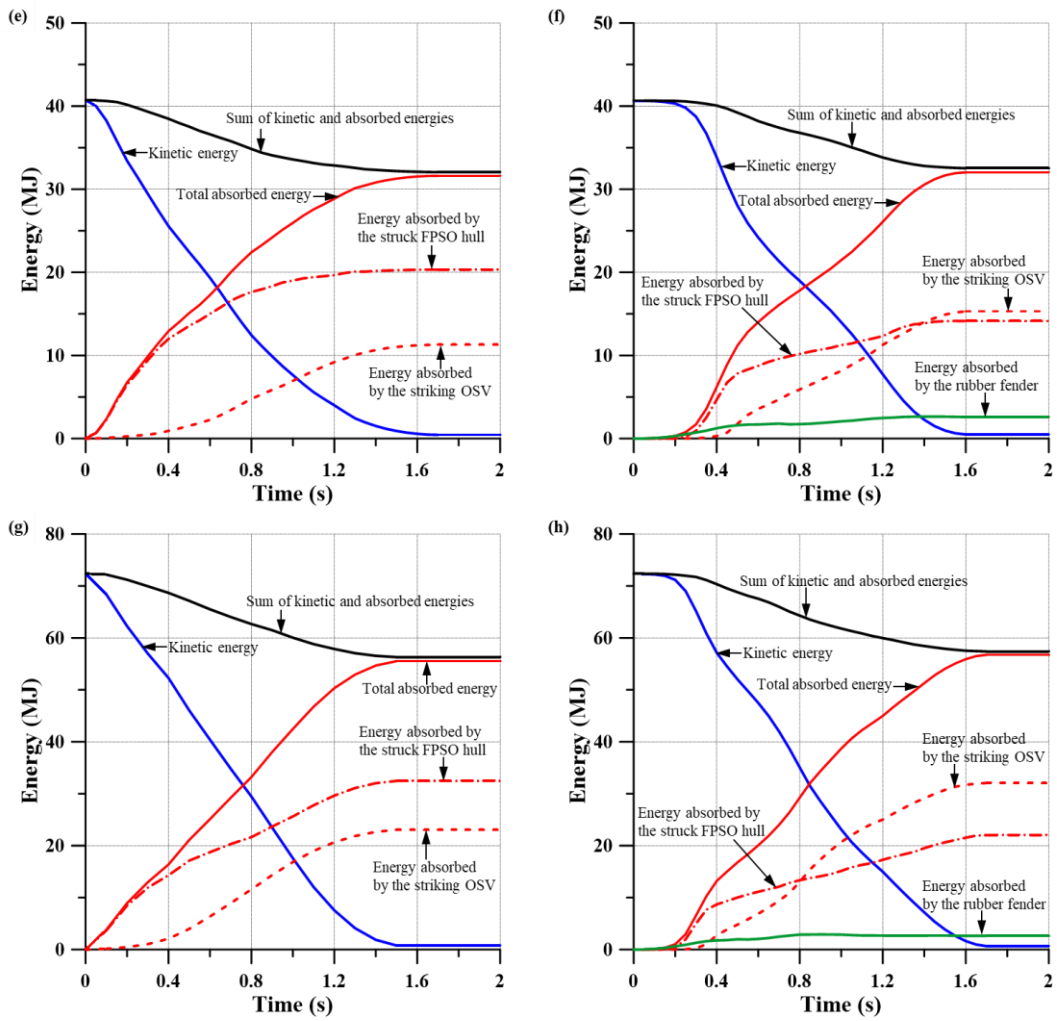
Figure A.2. Absorbed energy–time relation curves for a collision between the striking ship and struck ship at different collision speeds in the presence and absence of a rubber fender: Scenarios with a collision speed of 2 kt (a) without and (b) with the rubber fender, 4 kt (c) without and (d) with the rubber fender, 6 kt (e) without and (f) with the rubber fender, 8 kt (g) without and (h) with the rubber fender.